Marine Geology 276 (2010) 30–41

Contents lists available at ScienceDirect

Marine Geology

journal homepage: www.elsevier.com/locate/margeo

Margin architecture and seismic attenuation in the central Costa Rican forearc

J. Zhu *, H. Kopp, C. Papenberg, D. Klaeschen, E.R. Flueh, L. Planert

Leibniz-Institute of Marine Sciences (IFM-GEOMAR) and SFB574, Wischhofstrasse 1-3, 24148 Kiel, Germany

ARTICLE INFO

Article history:
Received 23 January 2010
Received in revised form 3 July 2010
Accepted 12 July 2010
Available online 17 July 2010

Communicated by D.J.W. Piper

Keywords:
Seismic attenuation
Amplitude modeling
Décollement
Seismic tomography
Middle America Trench

ABSTRACT

Seismic attenuation across the central Costa Rican margin wedge is determined from amplitude analysis of wide-angle seismic data. Travel time and amplitude modeling are applied to ocean bottom hydrophones along two trench-parallel profiles, located 30 km (P21) and 35 km (P18) landward of the deformation front northeast of Quepos Plateau. Tomographic inversion images a progressively thinning margin wedge from the coast to the lower slope at the trench. A 1–1.5 km thick décollement zone with seismic velocities of 3.5–4.5 km/s is sandwiched between the margin wedge and the subducting Cocos plate. For strike line P21, amplitude modeling indicates a Qp value of 50–150 for the upper margin wedge with seismic velocities ranging from 3.9 km/s to 4.9 km/s. Along strike line P18, Qp values of 50–150 are determined with velocities of 4.3–5.0 km/s in the upper margin wedge, increasing to 5.1–5.4 km/s in the lower margin wedge. Quantitative amplitude decay curves support the observed upper plate Qp values. In conjunction with earlier results from offshore Nicoya Peninsula, our study documents landward decreasing attenuation across the margin wedge, consistent with a change in lithology from the sediment-dominated frontal prism to the igneous composition of the forearc middle prism.

1. Introduction

Seismic attenuation is an inherent property of wave propagation and a measure of the total energy loss when a seismic wave propagates through the earth. The amplitude and waveform characteristics of seismograms may be modeled using the reflectivity method (Fuchs and Mueller, 1971; Braile and Smith, 1975), adapted to the calculation of pressure or displacement waveforms and thus suitable for either hydrophone or seismometer refraction recordings (Kennett, 1977). We employ the seismic attenuation factor for the calculation of synthetic seismograms to investigate the effect of inelastic attenuation in the Costa Rican margin wedge northeast of the Quepos Plateau (Fig. 1).

The Pacific margin of Costa Rica is characterized by the subduction of the oceanic Cocos plate underneath the Caribbean plate and has been imaged along several refraction profiles deployed since 1996 (Ye et al., 1996; Stavenhagen et al., 1998; Christeson et al., 1999; Walther, 2003; Zhu et al., 2009). The age, thickness and seismic velocities of the downgoing plate vary from the Nicoya Peninsula in the northwest to the Osa Peninsula in the southeast (Fig. 1, inset). Whereas the thickness of the oceanic crust increases from 5–6 km in the northwest to up to 14 km in the southeast, the age decreases from 22–24 Ma to 15–18 Ma from NW to SE as inferred from the seafloor spreading anomalies (Barckhausen et al., 2001). Along most profiles, an upper mantle velocity of 8.0–8.1 km/s is revealed. An exception to this is the area underneath the Quepos plateau where upper mantle velocities of 7.6–7.8 km/s prevail. Comparably low mantle velocities are also imaged underneath the outer flank of the Cocos Ridge, where it has been attributed to remnants of mafic material in the upper mantle or a plume signature (Walther, 2003). The core of the forearc margin wedge incorporates a fragment of the Caribbean oceanic plateau (Nicoya complex) (Hauff et al., 1997; Sinton et al., 1997). This igneous rock unit forms the forearc basement and is covered by a sediment apron (Ye et al., 1996). Fronting this unit is the frontal prism, which consists of accreted upper plate sediment (von Huene et al., 2000).

To the southeast, from the tip of Nicoya Peninsula to the northern limit of Osa Peninsula, numerous bathymetric features dot the incoming plate and upon entry in the trench modulate forearc deformation and morphology (e.g. Dominguez et al., 1998; Ranero and von Huene, 2000; von Huene et al., 2000). In addition to tectonic erosion caused by the impinging bathymetric features (von Huene et al., 1995), outer forearc kinematics are characterized by widespread subsidence resulting from subduction erosion (Lallemand et al., 1992; Vannucchi et al., 2003), i.e. material removal from the base of the upper plate.

One of the major objectives of examining the lateral variations of Qp values is to evaluate lateral seismic velocity and physical state variations of the margin wedge. The seismic velocity structure of the Costa Rican margin wedge has been obtained by a number of

* Corresponding author. Now at: Key Laboratory of Marginal Sea Geology, South China Sea Institute of Oceanology, Chinese Academy of Sciences, Guangzhou 510301, China. Tel.: +86 20 89023155; fax: +86 20 89023135.
E-mail addresses: jzhu@ifm-geomar.de (J. Zhu), hkopp@ifm-geomar.de (H. Kopp), cpapenberg@ifm-geomar.de (C. Papenberg), dklaeschen@ifm-geomar.de (D. Klaeschen), eflueh@ifm-geomar.de (E.R. Flueh), lplanert@ifm-geomar.de (L. Planert).

0025-3227/$ – see front matter.
doi:10.1016/j.margeo.2010.07.004

refraction experiments (e.g. Ye et al., 1996; Stavenhagen et al., 1998; Christeson et al., 1999; Walther, 2003; Zhu et al., 2009) and reflects the tectonic segmentation into a frontal prism, middle prism and inner prism as introduced by von Huene et al. (2009). We expect Qp variations to define these tectonic segments. The high signal-to-noise ratio of the first arrivals of the seismic data presented here facilitates amplitude modeling, as peak amplitudes are clearly identifiable. In this study, we firstly use seismic tomography to verify the velocity structure along two dip lines P15 and P24 and two strike lines P18 and P21 located offshore central Costa Rica (Fig. 1). We then employ the reflectivity method to constrain attenuation and velocity gradients in the margin wedge along the two strike lines. We compare our results to previous investigations of seismic attenuation conducted offshore Nicoya Peninsula, approximately 210 km to the northwest of our lines (Christeson et al., 2000) (Fig. 1). The generally low Qp values of the margin wedge indicate a highly tectonized frontal and middle prism, characterized by a high degree of fracturing. The seismic attenuation variations from the frontal prism to the middle prism document the lateral variations in lithology and physical state of the rock units.

2. Wide-angle seismic data

In 2002, a total of 42 IFM-GEOMAR ocean bottom hydrophones (OBH) (Flueh and Bialas, 1996) and 22 ocean bottom seismometers (OBS) (Bialas and Flueh, 1999) were deployed along four seismic profiles located about 25 km northeast of the Quepos Plateau (Zhu et al., 2009) (Fig. 1). Instruments were deployed along two dip lines P15 and P24 and two strike lines P21 and P18 (Fig. 1). The two dip lines P15/P24 were shot with a G-gun cluster (total volume 1800 in.^{3}) whereas the data along the two strike lines P18/P21 were acquired using a 32 l Boltgun (1952 in.^{3}). Both source types generated a seismic signal with frequencies from 4 to 40 Hz. A trigger interval of 30 s at a speed of 3.5 knots resulted in an average shotpoint distance of 54 m. Instrument positions on the seafloor were determined by analysis of the water wave arrivals. A time- and offset-dependent frequency filter in addition to a predictive deconvolution was applied to improve data resolution. A total of 32,058 first arrival picks and 7789 secondary arrival picks from 61 stations were used as input to a tomographic inversion. Comparing the reciprocity of the travel times for all possible source–receiver pairs validated phase coherency. Picking of seismic phases was conducted manually, and picking errors were assigned on the basis of the dominant period of the phase as well as data quality. We assigned 50 ms picking uncertainties at near offsets and 70 ms at far offsets for the first arrivals, and 80 ms for secondary arrivals.

The refractions through the upper margin wedge (Pumw) and the lower margin wedge (Plmw) are clearly observed on the record sections (e.g. Figs. 2–4). Station OBH 53 records refracted arrivals through the oceanic crust (Poc) and the upper mantle (Pn) (Fig. 2). The reflections from the top (PtP) and the bottom (PbP) of the décollement zone are recorded on several stations (e.g. Figs. 2 and 4) as are the intracrustal reflections PiP and crust–mantle boundary reflections (PmP) (Figs. 3 and 4). All of these arrivals are incorporated in the tomographic inversion.

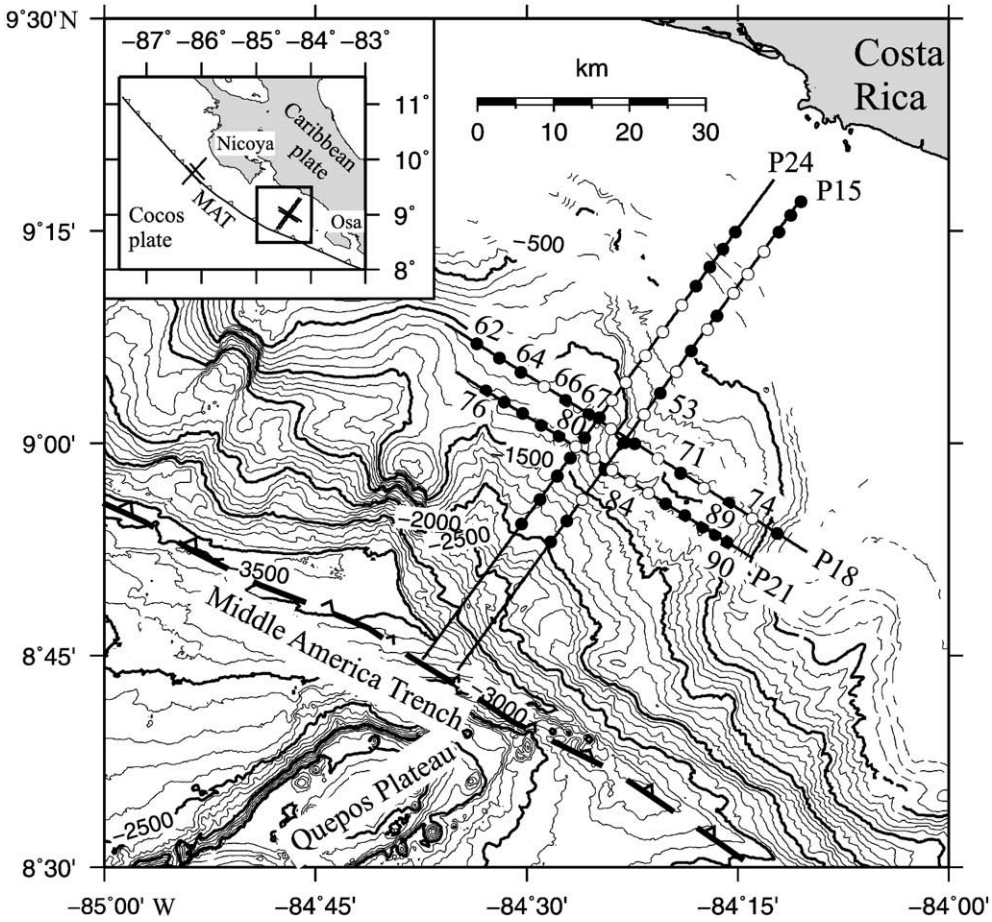

Fig. 1. Location map of seismic refraction profiles discussed in this study. Circles indicate positions of 40 ocean bottom hydrophones (OBH) (black) and 21 ocean bottom seismometers (OBS) (white) along the two strike and two dip lines. Stations used during amplitude modeling are marked by numbers. Seafloor topography is contoured at 100 m intervals. The inset map shows locations of the previous wide-angle seismic experiment by Christeson et al. (2000) offshore Nicoya Peninsula as well as this study. MAT: Middle America Trench.

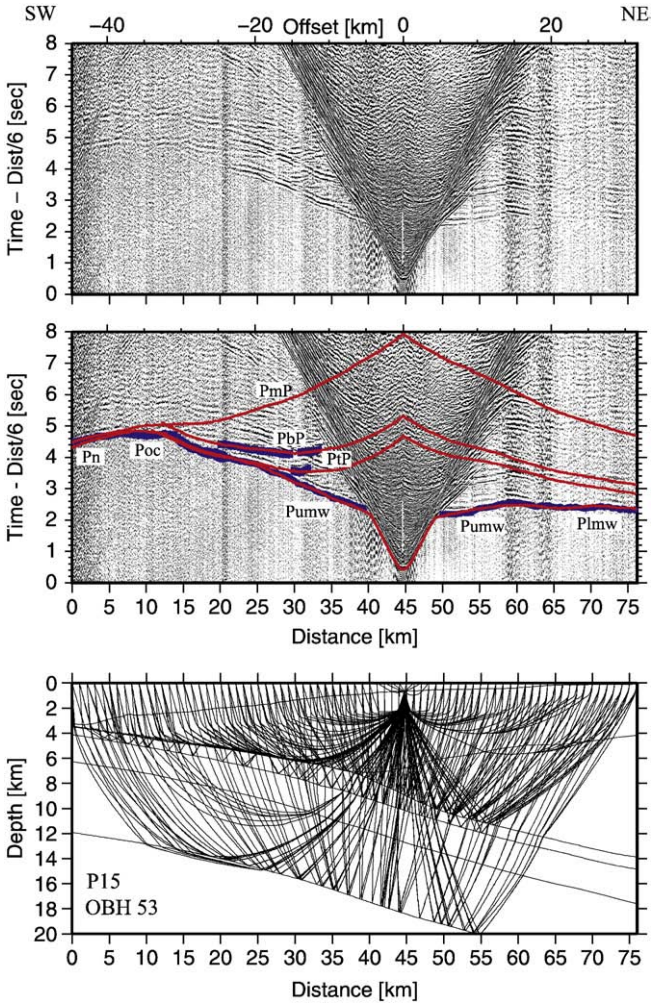

Fig. 2. Record section and ray paths for OBH 53 deployed on profile P15. Observed data are shown in the upper panel. Picked (blue line with picking error bars) and calculated travel times (red lines) are displayed in the center panel. Ray paths and phase abbreviations are shown in the lower panel. Refracted phase Pumw travels through the upper margin wedge and Plmw travels through the lower margin wedge. Poc is refracted through the oceanic crust. Reflection phase PtP tracks the top of the décollement zone and PbP tracks the bottom of this zone. PmP and Pn phases result from the oceanic crust–mantle boundary.

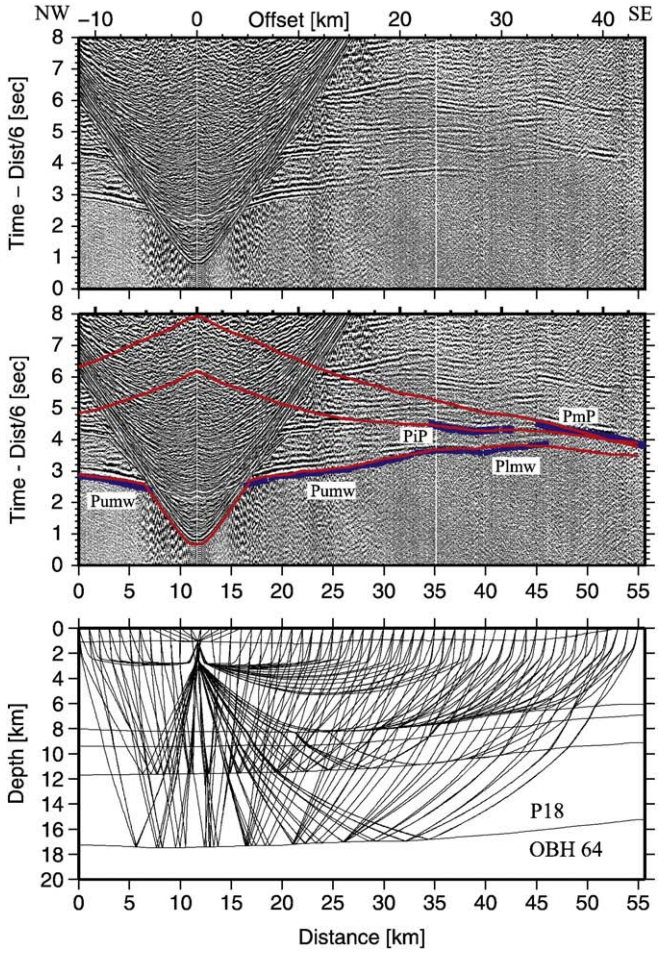

Fig. 3. Record section and ray paths for OBH 64 deployed on strike line P18. Reflection phase PiP originates at the boundary between oceanic layer 2 and layer 3. Please refer to Fig. 2 for display information and phase nomenclature.

3. Seismic travel time tomography

3.1. Method

The velocity–depth distribution of the seismic profiles is determined using the joint refraction and reflection travel time inversion method of Korenaga et al. (2000). The sedimentary section of the two dip lines (P15 and P24) has been modeled by forward ray tracing incorporating multichannel seismic reflection data (Zhu et al., 2009) and it is integrated in a starting model as a priori information. The fine mesh we apply in the tomographic inversion is better suited to resolve lateral variations in the short-wavelength structure compared to forward modeling. Lateral velocity variations, as observed e.g. in the upper margin wedge of our profile, are difficult to resolve using a layered model in the forward approach (Zhu et al., 2009). In Fig. 5a (profile distance 45–51 km), the high velocity variation within the upper margin wedge imaged by the tomographic inversion is resolved as a robust feature as validated by resolution tests. For all profiles, first arrivals and reflection travel times from floating reflectors were inverted to retrieve the 2-D velocity field. The forward travel time calculation uses a hybrid approach based on the graph method and the ray-bending method (Moser et al., 1992). For the inversion, the velocity field is parameterized as a mesh of nodes hanging below the seafloor with laterally and vertically varying node spacing. Horizontal grid size is 0.25 km, whereas vertical grid size varies from 0.05 km at the top of the model to 0.2 km at the bottom. We used horizontal correlation lengths ranging from 2 km at the top to 8 km at the bottom and vertical correlation lengths varying from 0.5 km at the top to 2 km at the bottom. A floating reflector is represented as an array of linear segments, whose nodal spacing is independent of that used in the velocity grid. The horizontal coordinates of reflector nodes are fixed so that each node has only one degree of freedom in the vertical direction (Korenaga et al., 2000). To incorporate multiple reflectors in the inversion procedure, we used the top–bottom modeling strategy to update the velocity model, i.e. the final velocity model with the first reflector fixed by damping serves as the initial model for the second reflector and so on. In this study, we chose to invert four reflectors corresponding to (1) the décollement, (2) the oceanic basement, (3) the upper–lower oceanic crust boundary and (4) the crust–mantle boundary (Moho discontinuity).

3.2. Results of tomographic inversion and interpretation

3.2.1. Seismic structure

The marine forearc is dominated by the upper margin wedge with a high velocity gradient of 0.4/s, which decreases in the lower margin

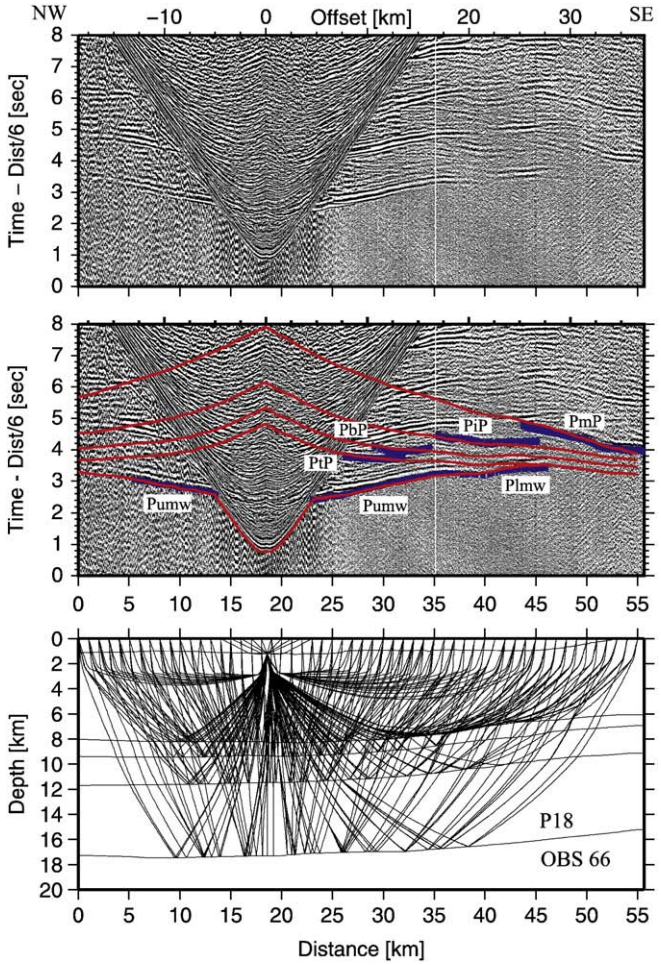

Fig. 4. Record section and ray paths for OBS 66 deployed on strike line P18. Please refer to Fig. 2 for display information and phase nomenclature.

wedge (Fig. 5). The tomographic images display laterally increasing seismic velocities within the margin wedge. Near the tip (Fig. 5, profile distance km 10–18), seismic velocities increase from 3 km/s to 4.5 km/s over the margin's thickness of ~2 km. From the middle slope to the upper slope, seismic velocities range from 4 km/s to 5.5 km/s and increase from 5.5 km/s to 6.5 km/s in the lower margin wedge. The subducting Caribbean oceanic plate is divided into two layers with distinct vertical velocity gradients: The upper layer is characterized by a large vertical velocity gradient, with velocities ranging from 5.0 km/s to 6.0 km/s and is identified as oceanic layer 2. The lower layer is traced by the 6 km/s isocontour at the top and the Moho interface with velocities of 7.2 km/s at the base and is considered to represent oceanic layer 3. A uniform thickness of 2 km and 5.5 km is observed for layers 2 and 3, respectively. Along all profiles, the décollement zone between the subducting Cocos plate and overriding Caribbean plate is characterized by a velocity inversion with a mean velocity of 4.0 km/s. The thickness of the décollement zone varies from ~1.0 km to ~1.5 km and is continuous up to our model boundaries.

The dense instrument spacing of 2.5 km to 3 km along the strike lines resolves fine structural variations of the margin wedge. Along strike line P18, 30 km from the deformation front, *P*-wave velocities of 4 km/s to 5.2 km/s are identified in the upper margin wedge where thickness variations do not exceed 1.5 km (Fig. 6a). The thin lower margin wedge shows velocities of 5.2 km/s to 5.5 km/s. The seismic structure of the margin wedge as imaged along P18 correlates to strike line P21, located 35 km from the deformation front (Fig. 6a). P21 displays an even more homogeneous structure, with layer thickness variations not exceeding 500 m and no considerable velocity variations (Fig. 6b). The structure of the lower plate is clearly two-dimensional, and velocities increase with depth and distance from the trench.

3.2.2. Model uncertainty and resolution tests

Using the inversion scheme described in Section 3.1, we have to consider two interrelated issues:

(1) The trade-off between depth and velocity parameters is linked to the reflected phase travel time inversion and depends on the source–receiver geometry. A conventional method to estimate the velocity–depth ambiguity is to perform sensitivity tests, such as checkerboard tests and Gaussian anomaly tests. In this procedure, different synthetic anomalies of various sizes are placed at specific positions in the models to assess at what point these anomalies are well resolved by the travel time inversion.

(2) Another issue is the uncertainty estimation in the velocity model, i.e. how well-resolved are the different parts of the model. This may be evaluated by estimating the influence of the initial model upon the obtained solution, as well as by estimating uncertainties applying a Monte Carlo analysis. The method involves a number of inversions with a variety of initial models using travel time picks with random errors applied. If all the Monte Carlo realizations have the same probability and if the initial models cover the full region of non-null probability within the space of parameters, the standard deviation of the obtained solutions can be interpreted as a measure of the final model parameter uncertainty.

To address the first issue, we conducted a resolution test by calculating synthetic data for a perturbed velocity model with a source–receiver geometry identical to the experiment setup. The synthetic data are then inverted with the initial unperturbed model to analyze how well the given perturbations are recovered. The perturbed velocity model is constructed using the final average velocity model with ±5% Gaussian anomalies placed at different positions in the model (Fig. 7). After 6 iterations, the position, shape and amplitude of the velocity anomalies are well recovered within the margin wedge and adequately recovered along the model periphery (Fig. 7). The relative high velocities found at profile distances of 45–52 km at around 4 km depth on profile 15 (Fig. 5a) in the margin wedge are a robust feature of the inversion solution.

Additionally, a nonlinear Monte Carlo uncertainty analysis (Tarantola and Valette, 1982) was conducted to estimate the model uncertainty and dependence of the obtained solutions on the initial model as addressed by the second issue mentioned above. The nonlinear Monte Carlo uncertainty was estimated as an a posteriori model covariance matrix (Tarantola, 1987), which can also be approximately expressed by the standard deviation of a number of Monte Carlo realizations (Korenaga et al., 2000). We constructed 100 Monte Carlo ensembles by inverting data with random errors with random initial velocity models (see Appendix). The 100 2-D initial velocity models were built by adding velocity values (randomly chosen between certain predefined limits) on a reference model beneath the basement. In addition, 100 noisy travel time data sets were constructed by adding random phase errors (±50 ms) and common-receiver errors (±50 ms) on the original data set (Zhang and Toksöz, 1998; Korenaga et al., 2000). Finally, each velocity model and corresponding reflector were inverted together with a noisy data set to estimate the influence of the starting model and the effect of realistic travel time errors. We used a top–bottom strategy to run the inversion step for each reflector, as described above. We added random velocities on the 2-D forward model of profile P24 including

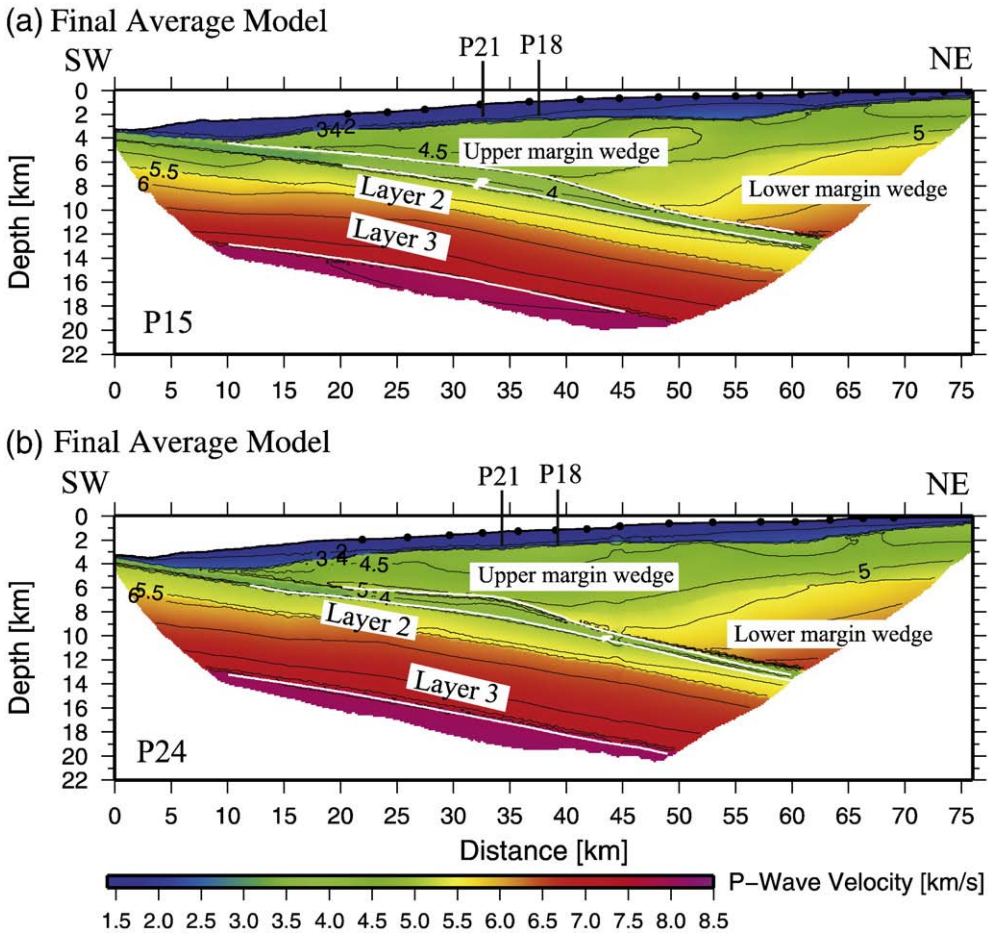

Fig 5. (a) Velocity–Depth distributions for profiles P15 (a) and P24 (b). The velocity models for P15 and P24 were derived by averaging 100 Monte Carlo ensembles for each line. The corresponding standard deviation of velocity and depth nodes for profile P24 is shown in Fig. 8. White lines mark reflectors. Contours are drawn at 0.5 km/s intervals.

two floating reflectors (top and base of the décollement zone, random variations within ±1 km) at the plate interface and one reflector (Moho, random variations within ±2 km) in the lower plate. One hundred input models were tested for each reflector during 10 iterations each, thus reducing the travel time root-mean-square misfits from several hundred milliseconds to about 70–90 ms. The average values and uncertainty of model parameters are obtained by averaging all Monte Carlo solutions and computing the corresponding standard deviation. The resulting deviation for profile P24 is shown in Fig. 8. Velocity uncertainties of the upper plate are usually lower than 0.15 km/s within the margin wedge (Fig. 8a, b). The largest velocity uncertainties occur within the low velocity décollement zone and reach 0.18 km/s here (Fig 8c). The depth uncertainties of the first and the second reflector reach about 500 m within the range of ray coverage. The velocity uncertainties within the subducting oceanic crust are comparable (0.06–0.15 km/s) (Fig. 8e, f). Uncertainties in Moho depth show values around ±1.5 km.

4. Reflectivity method

In this study, the amplitude modeling was performed using the 1D reflectivity code of Sandmeier and Wenzel (1986). The one-dimensional waveform modeling was exclusively applied to strike profiles P18 and P21 because the structural heterogeneity of the two dip lines prohibits one-dimensional modeling based on the reflectivity method along these transects. The 1-D initial velocity–depth model was provided by the tomography results of strike lines P18 and P21. The modeling procedure is a trial-and-error process in which we propose a model consisting of many plane homogeneous layers, each showing a distinct *P*-wave velocity (Vp), *S*-wave velocity (Vs), density (ρ), and *P* and *S* attenuation quality factors (Qp and Qs). Velocity gradients are approximated by a stack of layers with corresponding velocity contrasts. Calculated synthetic seismograms are compared with the observed seismograms, until an optimal fit is realized. For our amplitude modeling, we used a constant Poisson ratio of 0.28 and set Qp = 2Qs (as used by Spudich and Orcutt, 1980; Christeson et al., 2000). A Qp value of 300–500 for the crustal and sub-crustal environment is in agreement with earlier observations (Bowman, 1988). Densities were set to 1.5 g/cm^3 for the slope sediments and 1.8 g/cm^3 within the margin wedge (Kimura et al., 1997; Christeson et al., 2000). Densities for the oceanic crust were calculated using the relationship $\rho = 1.85 + 0.165$Vp (Christensen and Shaw, 1970; Christeson et al., 2000).

As the airgun source signature was unknown, we used a Fuchs-Mueller signal as input source wavelet. The source wavelet is defined by the equation given by Fuchs and Mueller (1971):

$$s(t) = \begin{cases} \sin \delta t - \frac{1}{m} \sin m\delta t, & 0 \le t \le T \\ 0 & t < 0, t > T \end{cases}$$

Where

$$\delta = \frac{N\pi}{T}, \quad m = \frac{N+2}{N}$$

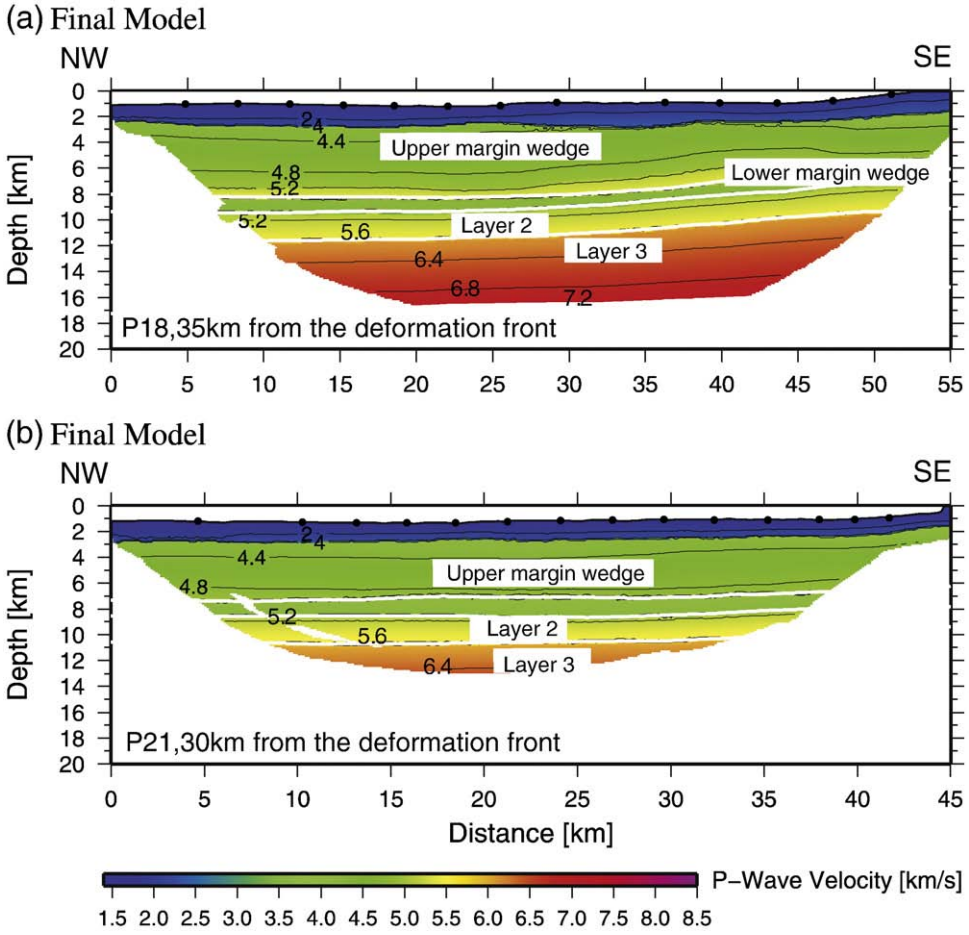

Fig 6. Velocity–Depth distributions for profiles P18 (a) and P21 (b) derived by tomographic inversion. White lines show reflectors. Contours are drawn at 0.4 km/s intervals.

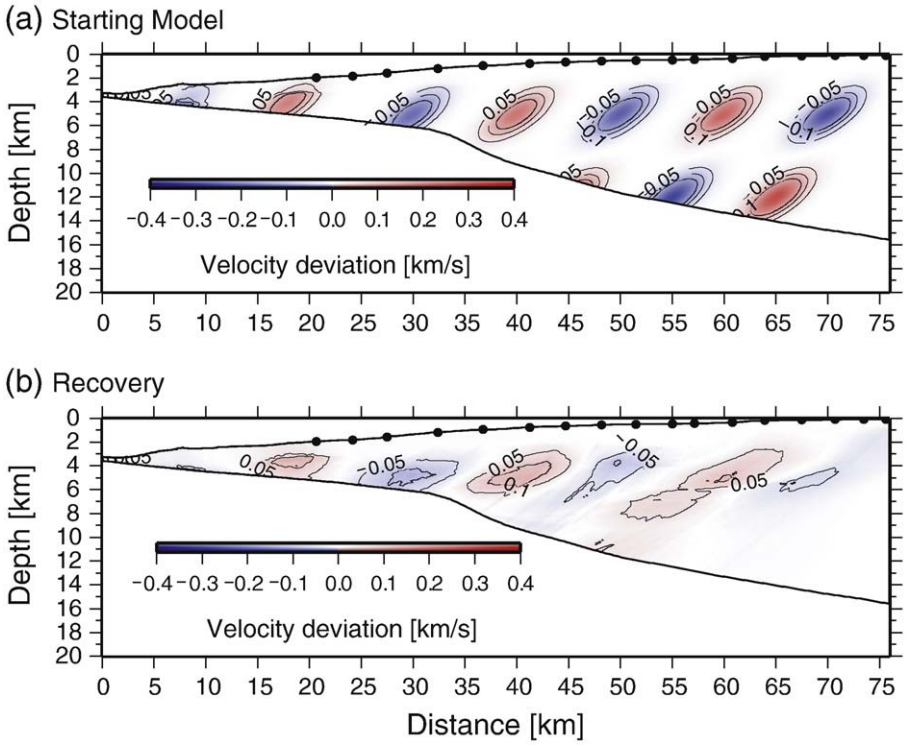

Fig 7. Upper plate resolution test for profile P15. (a) Velocity anomalies of ±5% in the synthetic model are given with respect to the initial velocity model. Velocity anomalies are applied to Gaussian anomalies rotated by 30 degrees. The source and receiver geometry used for synthetic travel time calculation is identical to the experiment layout. (b) Recovery obtained after 6 iterations.

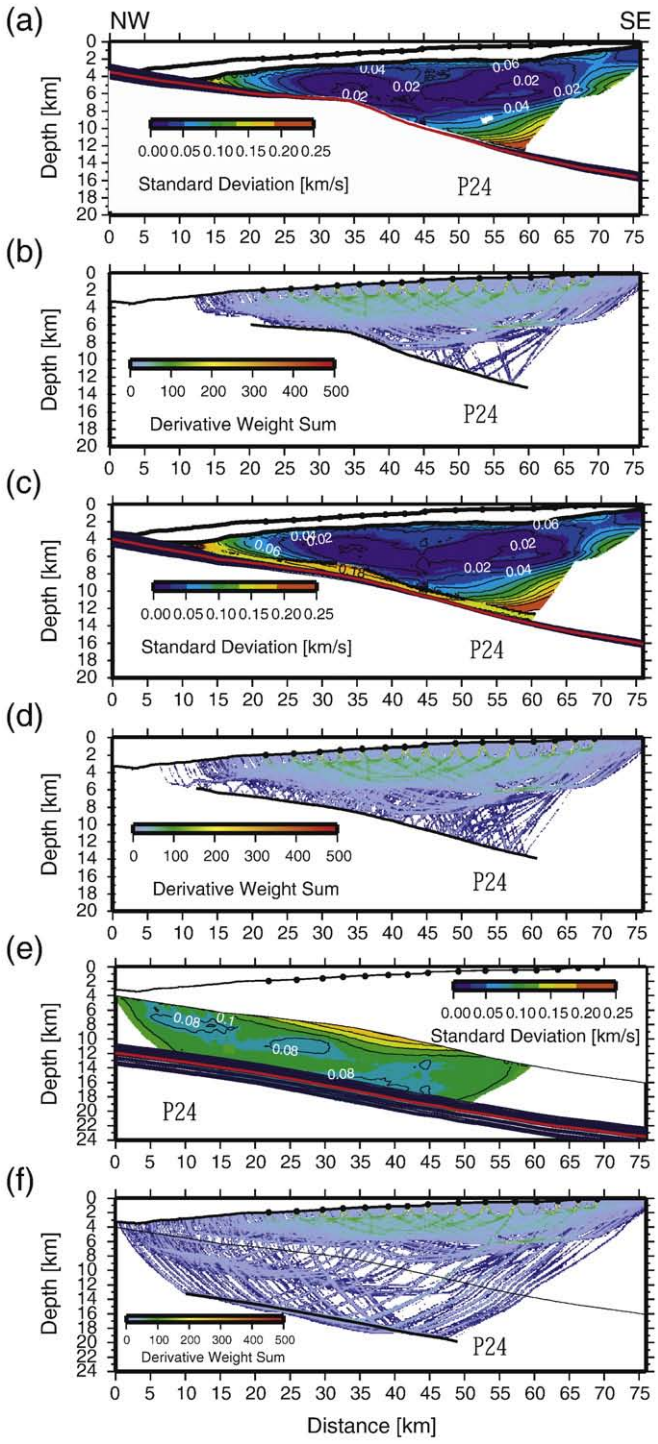

Fig 8. Standard deviations for velocity and reflector depth nodes of profile P24 derived from 100 Monte Carlo ensembles (a, c, e) and corresponding derivative weight sum from the average 100 realizations (b, d, f). Red lines show the average depth of reflectors and contours are drawn at 0.02 km/s intervals (a, c, e).

N is an integer defining the number of extrema and T is the duration of the wavelet in seconds. For our synthetic seismogram, $N=4$ and $T=0.4$ s were used. The frequency content of the Fuchs-Mueller signal used here has corner frequencies of 1/3–18/24 Hz, to simulate the dominant frequencies of the airgun signal recorded in the seismic section. Peak amplitudes of the refracted phases through the margin wedge are picked in the seismic record sections and synthetic seismograms along the two strike lines. The direct wave is used as reference to calibrate the amplitude data while considering the geometry spreading factors.

4.1. Strike lines P18 and P21

In our data, frequencies of the refracted waves in the margin wedge mainly focus between 5 Hz and 15 Hz, e.g. for OBS 68 in Fig. 9 (traces 200 to 330). Thus it is reasonable to use 12 Hz as the dominant frequency for the source signal during the amplitude modeling.

It is well known that the velocity gradient influences the amplitude of refracted phases (Banda et al., 1982). To verify the sensitivity of our analysis, we compare the amplitude behavior for varying velocity gradients for different Qp values (Fig. 10). We systematically vary the velocity gradient in the upper plate (margin wedge) according to the uncertainties obtained in Section 3.2.2 and then use the reflectivity method to calculate the synthetic seismograms and obtain the corresponding amplitude–distance curves (Fig. 10). The detailed model parameters are presented in Table 1. The resulting amplitude–distance curves show some variations in the near offset domain (offset<10 km), but at larger offsets, no significant variation conditional to different velocity gradients is observed (Fig. 10, models m1Q50, m2Q50 and m3Q50). The variations at near offsets are likely mainly related to interference from reflection phases here. The velocity model m1 corresponds to the velocity distribution retrieved by the tomographic inversion as was thus chosen to test the effect of increasing Qp values (Qp of 50, 75, 100, 150, and 200) on the amplitudes (Fig. 10, Table 1). The resulting curves in Fig. 10 show a relative sensitivity to the analyzed Qp range. Consequently, we assume that the velocity gradient has a relatively minor influence on our investigation (especially at offset>10 km), which is expressed within the general uncertainty (Fig. 10).

Two record sections along the strike lines P18 and P21 are shown in Fig. 11. The locations of OBS 84 and OBH 67 are indicated in Fig. 1. The primary travel time characteristic of the record section is interpreted as refracted arrivals through the margin wedge. First arrivals document both the velocities and Qp within the margin wedge and are clearly reproduced in the synthetic seismograms (Fig. 11a–b). We calculated synthetic seismograms using different attenuation (1/Qp) values and various vertical velocity gradients to test their effect on the seismic wave field. For OBS 84 displayed in Fig. 11a, the velocity–depth function of P21 (Fig. 11a, in panel vi) represents the margin wedge velocity, which is modestly slower (0.2–0.3 km/s) than the corresponding function determined by ray tracing (Fig. 6b) without including the effect of attenuation. Fig. 11b displays the original record section and synthetic seismograms calculated for OBH 67 of strike line P18. The primary arrivals through the upper margin wedge are focused between offsets 5 and 25 km (Fig. 11b). Again, synthetic seismograms are displayed for the different Qp values. For both profiles, it is difficult to define the proper Qp values from the synthetic seismograms, but a Qp of 300 yields unrealistically high amplitudes in the margin wedge compared to the real data (panels v in Fig. 11a, b). A quantitative estimation of Qp values is required as introduced below.

4.2. Quantitative estimations of Qp values

In order to estimate the Qp values of the upper plate in a quantitative manner, we analyze amplitude variations of first arrivals from the margin wedge. The amplitude–offset decay curve is used as a criterion to assess the validity of different Qp models by comparing the amplitude characteristics of the observed data and synthetic models. The peak amplitude values of the refracted phase from the margin wedge are picked manually using the Hampson-Russell software. This method is applied to the record sections indicated in Fig. 1. A prerequisite of this approach is the calibration of amplitudes,

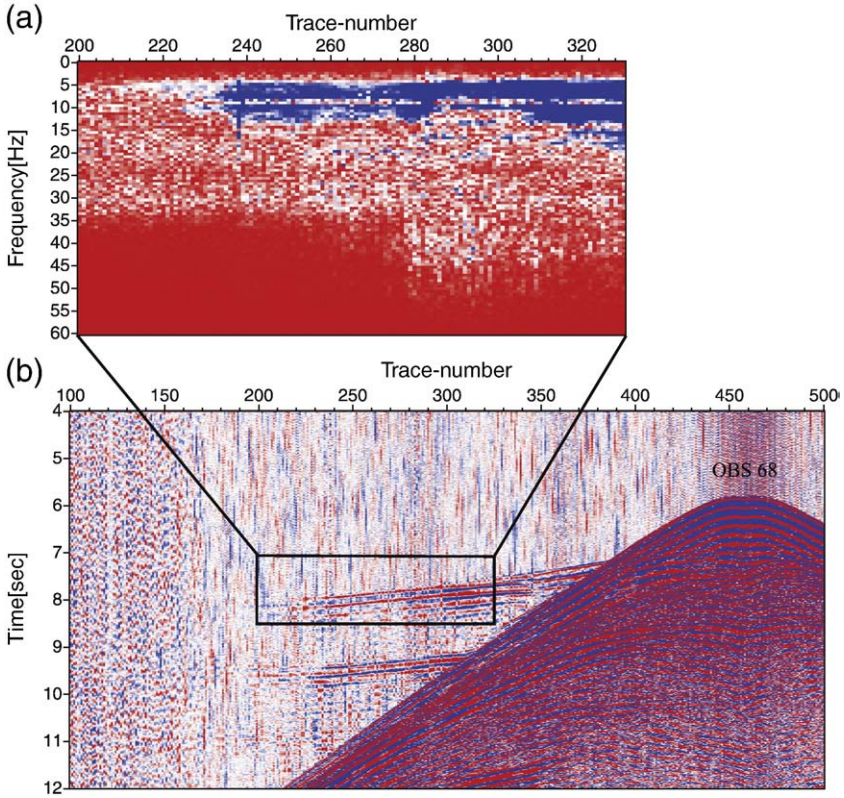

Fig. 9. Frequency spectrum of OBS 68. (a) Trace numbers from 200 to 330, (b) time domain data of OBS 68. The square area shows the time window from 7 s to 8.5 s used for the frequency spectrum.

usually with reference to the direct/water wave. The peak amplitudes of the direct wave from the synthetic seismograms and real data are matched firstly by applying geometric spreading corrections, and are then applied to the refracted phase. The relative amplitude curves are presented in Fig. 12. The amplitudes of the synthetic data decrease fairly smoothly with distance, whereas the recorded data show a rougher variation mainly caused by the complexity of the subsurface generating signal interference compared to the smooth phase of the synthetic model. The lower signal-to-noise ratio of the recorded data will enhance this scattering. In addition, although the tomographic images for lines P18 and P21 suggest a fairly smooth structure, the recorded data obviously are not one-dimensional and thus will to some degree violate the most important prerequisite for amplitude modeling. For this reason we conducted the modeling for two profiles at a distance of only approximately 5 km from each other to circumnavigate possible 3-D effects and minimize the effect statistically. For OBS 84, OBH 89, and OBH 90 of strike line P21, a Qp value of 50–150 generates comparable amplitudes between the observed and synthetic data (Fig. 12a–c). On average and for offsets greater than 10 km, the amplitude–distance curves of these record sections trend along the Qp = 75 synthetic curve. For OBS 68, OBH 71, and OBS 74 of strike line P18, a Qp value of 50–150 best produces similar amplitude characteristics between the observed and synthetic data (Fig. 12d–f).

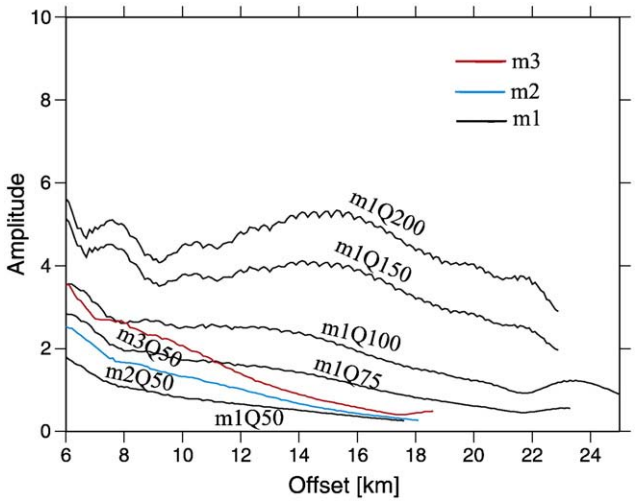

Fig. 10. Amplitude–Distance curves for models m1, m2, and m3 (different positive velocity gradients, see Table 1 for model parameters). Amplitude–Distance curves of m1 model with different Qp values are displayed.

4.3. Uncertainty estimations of the seismic attenuation

The forward amplitude modeling conducted for the two strike lines returns modest Qp values of 50–150, which correlate with the observed wavefield and amplitude–distance curves along profiles P18 and P21. Higher Qp values (> 200) in the margin wedge will

Table 1
Model parameters.

Model	Thickness of margin wedge (km)	Vp (km/s)	Velocity gradients of layers (km/s/km)
m1	4.46	4.0–4.8	0.18
m2	4.46	3.8–4.8	0.224
m3	4.46	3.9–5.2	0.269

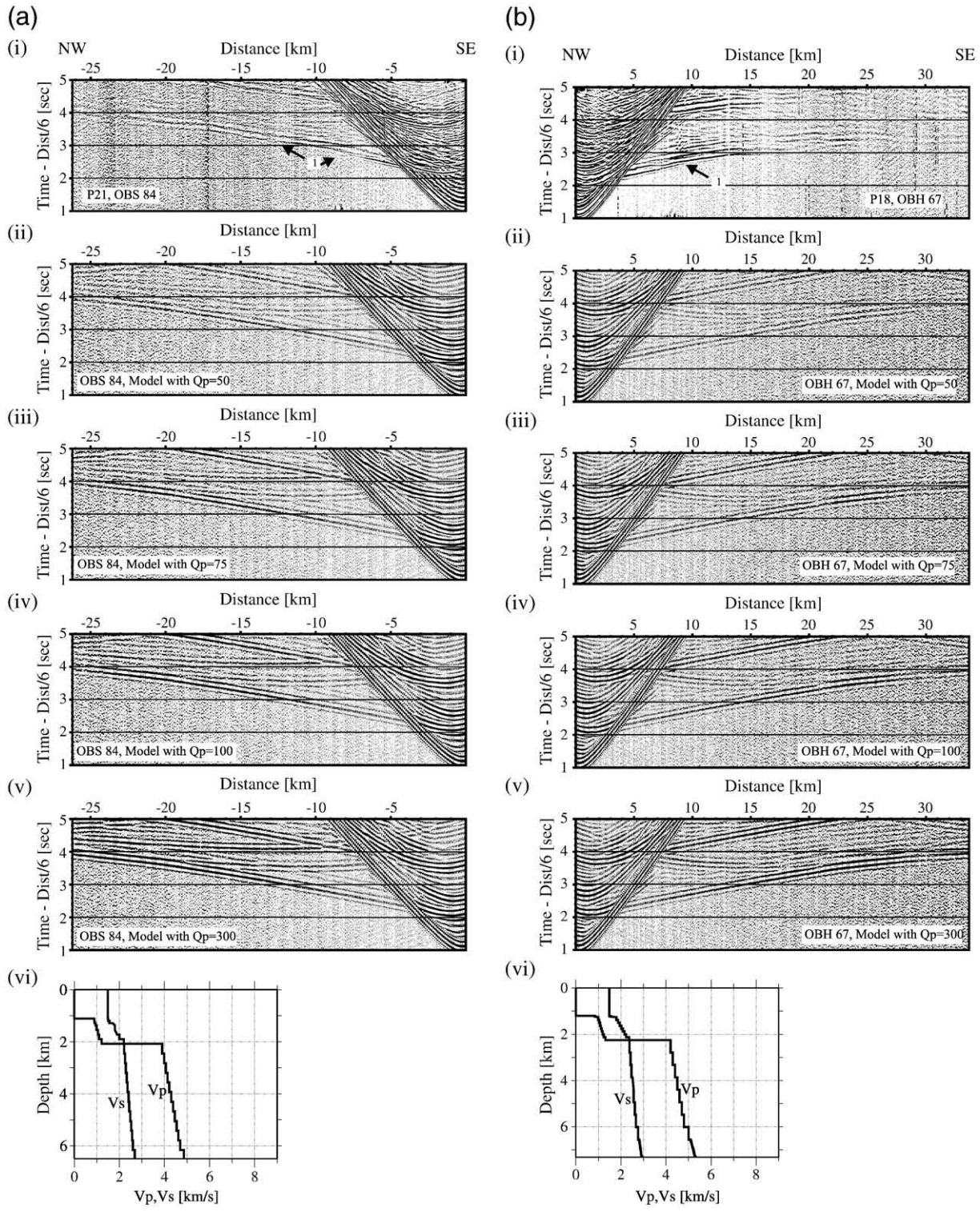

Fig. 11. Record section and synthetic seismograms of strike line P18 and P21. Ambient noise has been added to the synthetic record sections. Increasing Qp values of 50, 75, 100, and 300 within the margin wedge are shown in panels ii–v. The velocity–depth function is shown in panel vi. (a) OBS 84, (b) OBH 67.

generate high peak amplitude values at the related offset (Fig. 12) and will not reproduce a comparable amplitude behavior between the observed and synthetic data. A similar pattern is observed for all stations modeled on the two strike lines, where overestimated Qp values generate artificially high amplitude arrivals. The less homogeneous velocity distribution and structure of line P18 as discussed in Section 3.2.1 leads to a higher degree of scattering in the amplitude–distance curves of OBS 68, OBH 71, and OBS 74 (Fig. 12), however, the general trend of all curves on average will not exceed Qp values of 200.

In addition to the upper plate Qp values, other factors affecting the modeled amplitude pattern include the vertical velocity gradient of

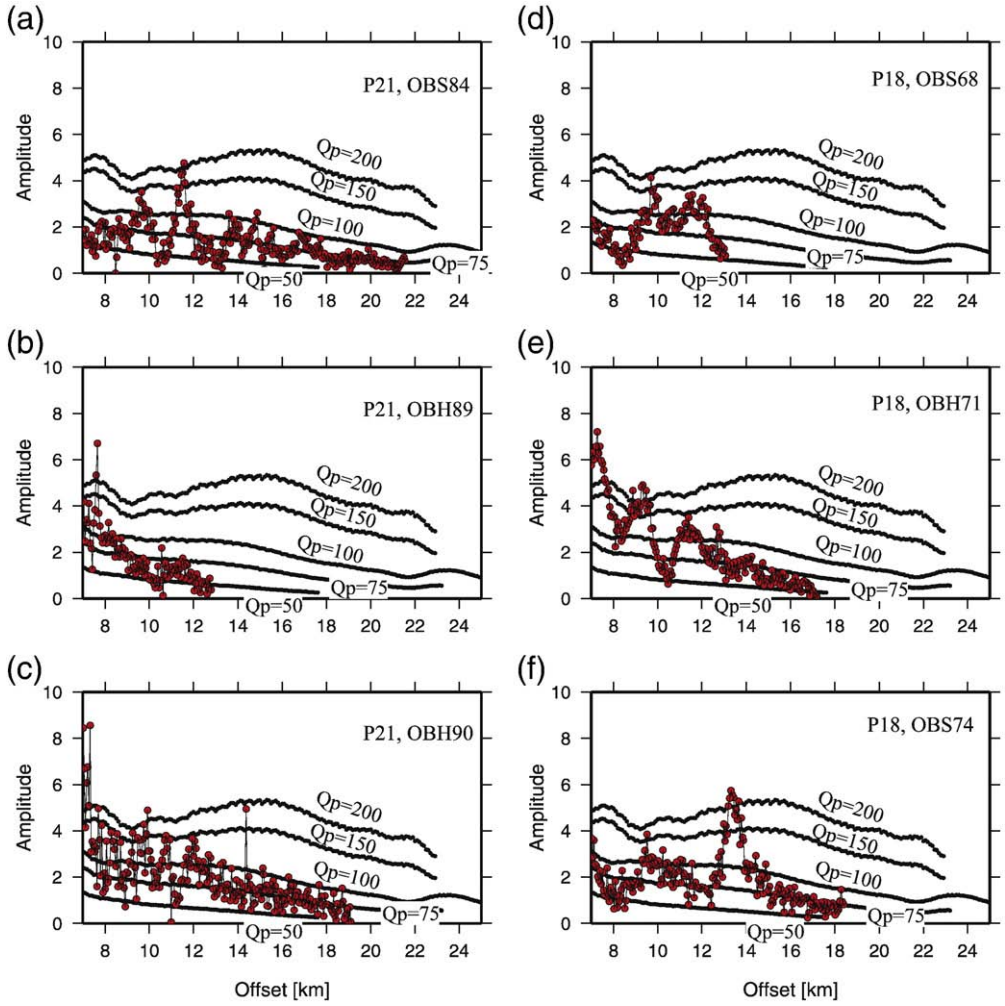

Fig. 12. Amplitude versus offset variations for refracted phases through the margin wedge of stations OBS 84, OBH 89, and OBH 90 along strike line P21, and OBS 68, OBH 71 and OBS 74 along the strike line P18. Red dotted lines show the amplitude decay curves of the record sections. Black lines show a constant Qp of 50, 75, 100, 150, and 200 in the margin wedge.

the margin wedge as discussed in Section 4.1. A high velocity gradient in the margin wedge (e.g. m3 model, velocity gradient of 0.269/s, Table 1) generates relative high amplitudes at corresponding offsets with an identical Qp of 50. Therefore, high vertical velocity gradients will lead to an underestimation of Qp values. The amplitude of the refracted phase can be decreased by either a decrease in the vertical velocity gradient or a decrease in the margin wedge Qp values. In order not to overestimate upper plate Qp values, we chose a vertical velocity gradient of 0.18/s (m1 model, Table 1) for the margin wedge consistent with the result of the tomographic inversion, yielding a minimum Qp value here (Fig. 12).

For station OBS 84 and OBH 90 of profile P21 (Fig. 12a, c), the amplitude–distance curves at offsets greater than 14 km closely correlate with the Qp = 75 curve. Scattering is higher at the near offsets, which are more affected by the larger variation of physical properties in the sedimentary cover as well as by interference of sediment reflections. This effect is also observed for station OBH 89 of the same line (Fig. 12b), however amplitudes could only be picked up to an offset of 13 km, impeding the analysis. Even more difficult to analyze due to the lack of far offset amplitude values are the data of OBS 68 of profile P18 (Fig. 12d). As for OBH 89, the low signal-to-noise ratio of this station inhibited exact amplitude picking at offset>13 km. Both stations, however, seem to follow the general trend not to exceed Qp values of 200. For OBH 71 (Fig. 12e), the slope of the amplitude–distance curve does not match the synthetic values. This is associated with the velocity gradient and comparison with curve m3Q50 of Fig. 10 implies that the velocity gradient is not matched underneath this station. As discussed in Section 4.1, the gradient will influence the slope of the curve but is less sensitive to the relative amplitude values. Data of OBS 74 (Fig. 12f) mainly trend around Qp = 75 and show a decisive maximum at 12–14 km offset. We interpret this peak to be caused by a low signal-to-noise ratio in the original data and thus to be artificial.

5. Discussion

The results of the tomographic inversion reveal more details of the seismic structure in the model space compared to the forward modeling results (Zhu et al., 2009). The fine shear mesh of velocity nodes of the velocity field indicates the *P*-wave velocity variation from 4.0–4.5 km/s at the tip of the margin to 4.1–6.5 km/s near the coast (Fig. 5). The thickness of the margin wedge increases at the trench axis from several hundred meters to about of 15 km at the coast (Fig. 5). Similar structural units as observed here (upper and lower margin wedge) are also resolved along the north Ecuador–south Colombia margin (Agudelo et al., 2009), where a significant accretionary wedge is missing.

The décollement zone is imaged as a 1–1.5 km thick low velocity zone sandwiched between the margin wedge basement and the subducting Cocos plate. The velocity model of dip lines P15 reveals a zonation of the décollement zone with velocities rapidly increasing from 3.0 km/s to 3.5 km/s from the deformation front over a distance of 15 km (P15). Velocities then remain constant (~3.5–3.6 km/s between 20 and 35 km offset) until they increase again underneath the lower margin wedge (~4.2 km/s at 50 km offset) (this velocity increase is not unambiguously resolved for P24). A similar velocity pattern of the underthrust material has also been reported for the erosional south Ecuadorian margin (Calahorrano et al., 2008), where a clear segmentation of the décollement zone could be inferred from pre-stack depth migrated multichannel seismic data. The progressively increasing seismic velocities concur with a reduction in porosity resulting from sediment compaction associated with fluid drainage.

The amplitude of a refracted seismic wave is controlled by the velocity of the medium through which it propagates as well as by the anelastic attenuation characteristics of the medium. The degree of cracking and water or gas in fractures will directly influence seismic attenuation by reducing Qp values (Bourbiè et al., 1987). This is consistent with the observation that Qp values generally increase with depth in the oceanic crust, which is attributed to the decrease in fracturing and structural heterogeneity (Wilcock et al., 1995).

In Costa Rica, previous studies have reported high attenuation (Qp = 25–50) approximately 10 km landward of the deformation front offshore Nicoya Peninsula (about 210 km northwest of our study area) (Christeson et al., 2000). These values are consistent with the low Qp values from marine sediment (Qp = 25–30) (Hamilton, 1972) and reflect the sedimentary composition of the highly tectonized frontal prism. This frontal prism is present along the entire ~500 km Costa Rican margin (von Huene et al., 2009) and is self-limiting in size, which is a function of material supply, convergence rate and taper. The width of the frontal prism off Costa Rica does not exceed 15 km landward of the deformation front. Approximately 20 km from the deformation front, Christeson et al. (2000) observed Qp values of 50–75, which is only slightly lower than our results from strike lines P21 and P18, located 30 km and 35 km from the trench, respectively (Fig. 1). The lower attenuation of our lines (Qp = 50–150) compared to the values (Qp = 25–50) recorded on the frontal prism (Christeson et al., 2000, Table 2) reflects the tectonically more stable domain of the middle prism and a change in lithology. The values are consistent with a Nicoya complex composition of the central Costa Rican margin wedge. The Nicoya complex is exposed on Nicoya Peninsula as ophiolitic rocks, composed of massive flows, pillows, dikes, basaltic breccias, gabbros, plagiogranites and radiolarian chert (Kuijpers, 1980). This unit has been interpreted as the seaward extent (Ye et al., 1996; Christeson et al., 1999) of the Caribbean Cretaceous oceanic plateau (Bowland and Rosencrantz, 1988; Sinton et al., 1997). Though attenuation across the middle prism decreases relative to the frontal prism, Qp values remain comparatively low. This may be associated to the fracturing of the middle prism, which has been documented in numerous studies. Faults penetrate deep into the slope sediment and into the basement rock (McIntosh et al., 1993; Hinz et al., 1996; Ranero and von Huene, 2000). Seismic attenuation is influenced by the material composition, which is reflected in the Qp structure of the margin wedge. The increase in Qp values from the frontal prism, to the middle and inner prism allows assessment of the changes in lithology. The overall relative low Qp may be related to the fluid budget of the margin as expressed in fluid expulsion through mud volcanoes distributed along the margin wedge. The fault pattern is intrinsically related to the hydrogeological system of the margin where the majority of focused fluid seepage occurs on the middle slope (Ranero et al., 2008). Fluid flow constitutes one cause of attenuation, however, only at frequencies below the frequency range of our study (Toksöz et al., 1987).

Table 2
Margin wedge velocities and Qp values from wide-angle strike lines.

Region	Costa Rica, Nicoya Peninsula		Central Costa Rica	
Distances from trench	10 km	20 km	30 km	35 km
Velocity ranges (km/s)	4–4.4	4.4–4.8	3.9–4.9	4.2–5.0 (upper margin wedge) 5.1–5.4 (lower margin wedge)
Thickness of the margin wedge (km)	1.5	3.0	4–4.5	3.5–5 (upper margin wedge) 1–1.5 (lower margin wedge)
Qp	25–50	50–75	50–150	50–150

Reference Christeson et al., 2000 this study.

6. Conclusions

We apply the reflectivity method and incorporate the Q parameter to obtain a 1D model for Qp on the Costa Rican margin wedge (Table 2). By comparison with previous studies (Christeson et al., 2000) we document a lateral decrease of attenuation across the margin wedge with distance from the trench, implying physical and lithologic variations along the lower slope of the marine forearc. This is related to material strength variations associated with a change in lithology from the sediment-dominated frontal prism to the igneous composition of the middle prism of the forearc. Seismic velocities and Qp values of the margin wedge are consistent with a high degree of fracturing as suggested by previous studies (Ranero et al., 2008), which facilitates mass wasting and subduction erosion processes.

Acknowledgments

We are grateful to all colleagues and participants of Cruise SO163 for their help with data acquisition and processing, particularly to the skillful crew of the RV Sonne. We used the GMT software (Wessel and Smith, 1991) and Seismic Unix software package (Stockwell, 1999) to plot several figures. We also wish to thank Editor David J. W. Piper for providing a very useful pre-review of the manuscript and two anonymous reviewers whose suggestions contributed to improving the original manuscript. J.Z. gratefully acknowledges a scholarship granted by the German Academic Exchange Service (DAAD) and the financial support from the National Natural Science Foundation of China (40674051) and the Knowledge Innovation Program of the Chinese Academy of Sciences (SQ200910).

Appendix

1. Monte Carlo analysis

A practical way to estimate the model uncertainty for tomographic inversion is the Monte Carlo method (Tarantola and Valette, 1982; Tarantola, 1987; Korenaga et al., 2000). The nonlinear Monte Carlo uncertainty was estimated as an a posteriori model covariance matrix (Tarantola, 1987), which can also be approximately expressed by the standard deviation of a number of Monte Carlo realizations assuming that all realizations have the same probability (Korenaga et al., 2000). Commonly, 100 random initial velocity models are generated by adding the predefined random numbers to velocity values and depth ranges of a reflector on a 1-D reference model. In this study we modify a 2D forward modeling velocity field by adding the constant random values at the same layer and also modify the depths of the different

reflectors to construct 100 2D random velocity models. See main text for further information. The following chart presents the detailed process:

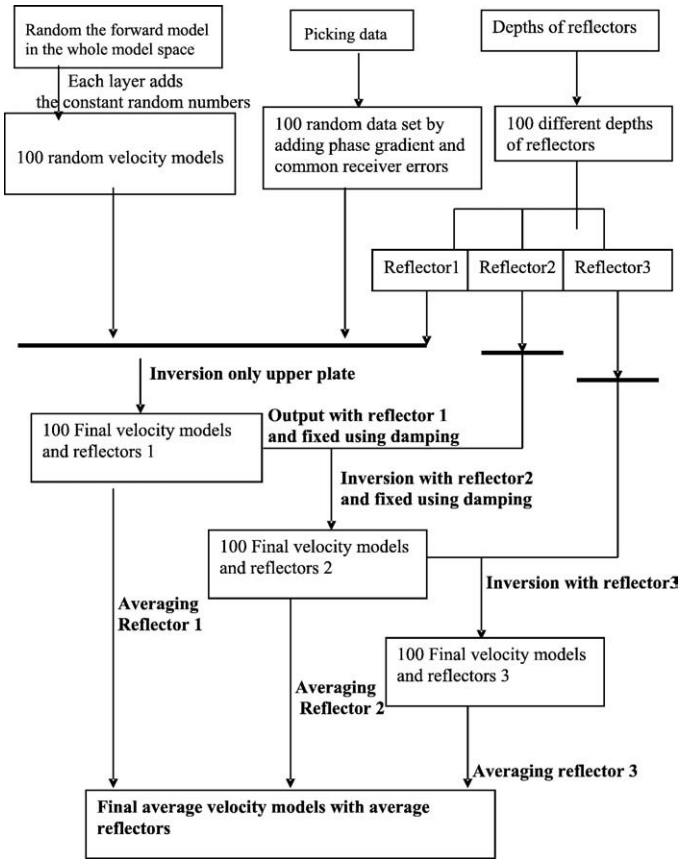

References

Agudelo, W., Ribodetti, A., Collot, J.-Y., Operto, S., 2009. Joint inversion of multichannel seismic reflection and wide-angle seismic data: Improved imaging and refined velocity model of the crustal structure of the north Ecuador–south Colombia convergent margin. Journal of Geophysical Research 114, B02306 doi:10.1029/2008JB005690.

Banda, E., Deichmann, N., Braile, L.W., Ansorge, J., 1982. Amplitude study of the Pg phase. Journal of Geophysics 51, 153–164.

Barckhausen, U., Ranero, C.R., von Huene, R., Cande, S.C., Roeser, H., 2001. Revised tectonic boundaries in the Cocos Plate off Costa Rica: implication for the segmentation of the convergent margin and for plate tectonic models. Journal of Geophysical Research 106, 19207–19220.

Bialas, J., Flueh, E.R., 1999. Ocean bottom seismometers. Sea Technology 40 (4), 41–46.

Bourbiè, T., Coussy, O., Zinszner, B., 1987. Acoustics of Porous Media. Gulf Publishing Company, Houston, Tex.

Bowland, C.L., Rosencrantz, E., 1988. Upper crustal structure of the western Colombian basin. Caribbean Sea, Geological Society America Bulletin 100, 534–546.

Bowman, J.R., 1988. Body wave attenuation in the Tonga subduction zone. Journal of Geophysical Research 93 (B3), 2125–2139.

Braile, L.W., Smith, R.B., 1975. Guide to the interpretation of crustal refraction profiles. Geophysical Journal of the Royal Astronomical Society 40, 145–176.

Calahorrano, B.A., Salleres, V., Collot, J.-Y., Sage, F., Ranero, C.R., 2008. Nonlinear variation of the physical properties along the southern Ecuador subduction channel: results from depth-migrated seismic data. Earth and Planetary Science Letters 267, 453–467.

Christensen, N.I., Shaw, G.H., 1970. Elasticity of mafic rocks from the Mid-Atlantic Ridge. Geophysical Journal of the Royal Astronomical Society 20, 271–284.

Christeson, G.L., McIntosh, K.D., Shipley, T.H., 2000. Seismic attenuation in the Costa Rica margin wedge: amplitude modeling of ocean bottom hydrophone data. Earth and Planetary Science Letters 179, 391–405.

Christeson, G.L., McIntosh, K.D., Shipley, T.H., Flueh, E.R., Goedde, H., 1999. Structure of the Costa Rica convergent margin, offshore Nicoya Peninsula. Journal of Geophysical Research 104, 25443–25468.

Dominguez, S., Lallemand, S.E., Malavieille, J., von Huene, R., 1998. Upper plate deformation associated with seamount subduction. Tectonophysics 293, 207–224.

Flueh, E.R., Bialas, J., 1996. A digital, high data capacity ocean bottom recorder for seismic investigations. International Underwater System Design 18 (3), 18–20.

Fuchs, K., Mueller, G., 1971. Computation of synthetic seismograms with the reflectivity method and comparison with observation. Geophysical Journal of the Royal Astronomical Society 23, 417–433.

Hamilton, E.L., 1972. Compressional-wave attenuation in marine sediments. Geophysics 37, 620–646.

Hauff, F., Hoernle, K., Schmincke, H.-U., Werner, R., 1997. A mid Cretaceous origin for the Galápagos hotspot: volcanological, petrological and geochemical evidence from Costa Rican oceanic crustal segments. Geologische Rundschau 86, 141–155.

Hinz, K., von Huene, R., Ranero, C.R., PACOMAR Group, 1996. Tectonic structure of the convergent Pacific margin offshore Costa Rica from multichannel seismic reflection data. Tectonics 15, 54–66.

Kennett, B.L.N., 1977. Towards a more detailed seismic picture of the oceanic crust and mantle. Marine Geophysical Researches 3, 7–42.

Kimura, G., Sliver, E., Blum, P., et al., 1997. Proceedings of the Ocean Drilling Program, Initial Report, vol. 170. Ocean Drilling Program, College Station, Texas. (458 p.).

Korenaga, J., Holbrook, W.S., Kent, G.M., Kelemen, P.B., Detrick, R.S., Larsen, H.-C., Hopper, J.R., Dahl-Jensen, T., 2000. Crustal structure of the southeast Greenland margin from joint refraction and reflection seismic tomography. Journal of Geophysical Research 105 (B9), 21591–21614.

Kuijpers, E.P., 1980. The geologic history of the Nicoya Ophiolitite Complex Costa Rica, and its geotectonic significance. Tectonophysics 68, 233–255.

Lallemand, S.E., Schnurle, P., Manoussis, S., 1992. Reconstruction of subduction zone paleogeometries and quantification of upper plate material losses caused by tectonic erosion. Journal of Geophysical Research 97, 217–239.

McIntosh, K., Silver, E., Shipley, T., 1993. Evidence and mechanisms for forearc extension at the accretionary Costa Rica convergent margin. Tectonics 12, 1380–1392.

Moser, T.J., Nolet, G., Snieder, R., 1992. Ray bending revisited. Bulletin. Seismological Society of America 82, 259–288.

Ranero, C.R., von Huene, R., 2000. Subduction erosion along the Middle America convergent margin. Nature 404, 748–752.

Ranero, C.R., Grevemeyer, I., Sahling, H., Barckhausen, U., Hesen, C., Wallmann, K., Weinrebe, W., Vannucchi, P., von Huene, R., McIntosh, K., 2008. Hydrogeological system of erosional convergent margins and its influence on tectonics and interplate seismogenesis. Geochemistry, Geophysics, Geosystems 9 (Q03S04) doi:10.1029/2007GC001679.

Sandmeier, K.J., Wenzel, F., 1986. Synthetic seismograms for a complex crustal model. Geophysical Research Letters 13, 22–25.

Sinton, C.W., Duncan, R.A., Denyer, P., 1997. Nicoya Peninsula, Costa Rica: a single suite of Caribbean oceanic plateau magmas. Journal of Geophysical Research 102 (B7), 15,507–15,520.

Spudich, P., Orcutt, J., 1980. Petrology and porosity of an ocean crustal site: results from wave form modeling of seismic refraction data. Journal of Geophysical Research 85 (B3), 1409–1433.

Stavenhagen, A.U., Flueh, E.R., Ranero, C.R., McIntosh, K.D., Shipley, T., Leandro, G., Schulze, A., Dañobeitia, J.J., 1998. Seismic wide-angle investigations in Costa Rica—a crustal velocity model from the Pacific to the Caribbean coast. Zentralblatt für Geological und Paläontologie, Teil I 3–6, 393–408.

Stockwell, J.W., 1999. The CWP/SU: Seismic Un*x package. Computers and Geosciences 25 (4), 415–419.

Toksöz, M.N., Wu, R.S., Schmitt, D.P., 1987. Physical mechanisms contributing to seismic attenuation in the crust. In: Erdik, M.O., Toksöz, M.N. (Eds.), Strong Ground Motion Seismology. D. Reidel Publishing Company, Dordrecht, pp. 225–247.

Tarantola, A., 1987. Inverse Problem Theory: Methods for Data Fitting and Model Parameter Estimation. Elsevier, New York (613 pp.).

Tarantola, A., Valette, B., 1982. Inverse problems = quest for information. Journal of Geophysics 50, 159–170.

Vannucchi, P., Ranero, C.R., Galeotti, S., Straub, S.M., Scholl, D.W., McDougall-Reid, K., 2003. Fast rates of subduction erosion along the Costa Rica Pacific margin: implications for nonsteady rates of crustal recycling at subduction zones. Journal of Geophysical Research 108 (B11), 2511 doi:10.1029/2002JB002207.

von Huene, R., Bialas, J., Flueh, E., Cropp, B., Csernok, T., Fabel, E., Hoffmann, J., Emeis, K., Holler, P., Jeschke, G., Leandro, M.C., Perez Fernandes, I., Chavarria, S.J., Florez, H.A., Escobado, Z.D., Leon, R., Barrios, L.O., 1995. Morphotectonics of the Pacific convergent margin of Costa Rica. In: Mann, P. (Ed.), Geologic and Tectonic Development of the Caribbean Plate Boundary in Southern Central America: Geological Society of America, Special Paper, vol. 295, pp. 291–307.

von Huene, R., Ranero, C.R., Weinrebe, W., 2000. Quaternary convergent margin tectonics of Costa Rica, segmentation of the Cocos Plate, and Central American volcanism. Tectonics 19, 314–334.

von Huene, R., Ranero, C.R., Scholl, D.W., 2009. Convergent margin structure in high quality geophysical images and current kinematic and dynamic models. In: Lallemand, S., Funiciello, F. (Eds.), Subduction Zones Geodynamics. : Frontiers in Earth Sciences, vol. 2, XXII. Springer, Berlin, Heidelberg, pp. 137–157.

Walther, C.H.E., 2003. The crustal structure of the Cocos ridge off Costa Rica. Journal of Geophysical Research 108 (B3), 2136 doi:10.1029/2001JB000888.

Wessel, P., Smith, W.H.F., 1991. Free software helps map and display data. EOS. Transactions of the American Geophysical Union 72, 445–446.

Wilcock, W.S.D., Solomon, S.C., Purdy, G.M., Toomey, D.R., 1995. Seismic attenuation structure of the East Pacific Rise near 9°30′N. Journal of Geophysical Research 100 (B12), 24147–24165.

Ye, S., Bialas, J., Flueh, E.R., Stavenhagen, A., von Huene, R., Leandro, G., Hinz, K., 1996. Crustal structure of the Middle American trench off Costa Rica from wide-angle seismic data. Tectonics 15, 1006–1021.

Zhang, J., Toksöz, M.N., 1998. Nonlinear refraction traveltime tomography. Geophysics 63, 1726–1773.

Zhu, J., Kopp, H., Flueh, E.R., Klaeschen, D., Papenberg, C., Planert, L., 2009. Crustal structure of the central Costa Rica subduction zone: implications for basal erosion from seismic wide-angle data. Geophysical Journal International 178, 1112–1131.